High-entropy (Nd0.2Sm0.2Eu0.2Y0.2Yb0.2)4Al2O9 with good high temperature stability, low thermal conductivity, and anisotropic thermal expansivity

Zifan ZHAO
Science and Technology on Advanced Functional Composite Laboratory, Aerospace Research Institute of Materials & Processing Technology, Beijing 100076, China School of Engineering and Technology, China University of Geosciences, Beijing 100083, China

Huimin XIANG
Science and Technology on Advanced Functional Composite Laboratory, Aerospace Research Institute of Materials & Processing Technology, Beijing 100076, China

Heng CHEN
Science and Technology on Advanced Functional Composite Laboratory, Aerospace Research Institute of Materials & Processing Technology, Beijing 100076, China

Fu-Zhi DAI
Science and Technology on Advanced Functional Composite Laboratory, Aerospace Research Institute of Materials & Processing Technology, Beijing 100076, China

Xiaohui WANG
Shenyang National Laboratory for Materials Science, Institute of Metal Research, Chinese Academy of Sciences, Shenyang 110016, China
Follow this and additional works at: https://dc.tsinghuajournals.com/journal-of-advanced-ceramics

See next page for additional authors

Recommended Citation

High-entropy (Nd0.2Sm0.2Eu0.2Y0.2Yb0.2)4Al2O9 with good high temperature stability, low thermal conductivity, and anisotropic thermal expansivity

Authors

Zifan ZHAO, Huimin XIANG, Heng CHEN, Fu-Zhi DAI, Xiaohui WANG, Zhijian PENG, and Yanchun ZHOU

Research Article

High-entropy $(Nd_{0.2}Sm_{0.2}Eu_{0.2}Y_{0.2}Yb_{0.2})_4Al_2O_9$ with good high temperature stability, low thermal conductivity, and anisotropic thermal expansivity

Zifan ZHAO[a,b], Huimin XIANG[a], Heng CHEN[a], Fu-Zhi DAI[a],
Xiaohui WANG[c], Zhijian PENG[b,*], Yanchun ZHOU[a,*]

[a]*Science and Technology on Advanced Functional Composite Laboratory, Aerospace Research Institute of Materials & Processing Technology, Beijing 100076, China*
[b]*School of Engineering and Technology, China University of Geosciences, Beijing 100083, China*
[c]*Shenyang National Laboratory for Materials Science, Institute of Metal Research, Chinese Academy of Sciences, Shenyang 110016, China*

Abstract: The critical requirements for the environmental barrier coating (EBC) materials of silicon-based ceramic matrix composites (CMCs) include good tolerance to harsh environments, thermal expansion matches with the interlayer mullite, good high-temperature phase stability, and low thermal conductivity. Cuspidine-structured rare-earth aluminates $RE_4Al_2O_9$ have been considered as candidates of EBCs for their superior mechanical and thermal properties, but the phase transition at high temperatures is a notable drawback of these materials. To suppress the phase transition and improve the phase stability, a novel cuspidine-structured rare-earth aluminate solid solution $(Nd_{0.2}Sm_{0.2}Eu_{0.2}Y_{0.2}Yb_{0.2})_4Al_2O_9$ was designed and successfully synthesized inspired by entropy stabilization effect of high-entropy ceramics (HECs). The as-synthesized HE $(Nd_{0.2}Sm_{0.2}Eu_{0.2}Y_{0.2}Yb_{0.2})_4Al_2O_9$ exhibits a close thermal expansion coefficient ($6.96\times10^{-6}\,K^{-1}$ at 300–1473 K) to that of mullite, good phase stability from 300 to 1473 K, and low thermal conductivity ($1.50\,W\cdot m^{-1}\cdot K^{-1}$ at room temperature). In addition, strong anisotropic thermal expansion has been observed compared to $Y_4Al_2O_9$ and $Yb_4Al_2O_9$. The mechanism for low thermal conductivity is attributed to the lattice distortion and mass difference of the constituent atoms, and the anisotropic thermal expansion is due to the anisotropic chemical bonding enhanced by the large size rare-earth cations.

Keywords: $(Nd_{0.2}Sm_{0.2}Eu_{0.2}Y_{0.2}Yb_{0.2})_4Al_2O_9$; high-entropy ceramics (HECs); environmental barrier coatings; phase stability; thermal properties

1 Introduction

Silicon-based ceramics such as Si_3N_4 and SiC_f/SiC ceramic matrix composites (CMCs) have been considered as candidates to replace superalloys to manufacture the hot section structural components in gas turbine engines due to their superior high-temperature mechanical properties, good durability, and excellent creep- and oxidation-resistance [1–6]. However, a key barrier to realizing silicon-based turbine hot section structural

components is the lack of environmental durability in combustion environments because the protective silica scale on the surface of silicon-based ceramics can be corroded by high-temperature water vapor and yields volatile products, such as $Si(OH)_4$, which will result in the rapid recession [7–11]. Thus, environmental barrier coatings (EBCs) are necessary for silicon-based ceramics, which can protect the hot section structural components from the corrosion of high-temperature water vapor [12,13].

Generally, the current prime EBC system of Si_3N_4 and SiC_f/SiC CMCs consists of a multiple-layer silicon/mullite/refractory oxide coating structure and each layer is under a specific purpose. Silicon as the adhesive layer bonds the substrate and the upper coatings, mullite as the interlayer reduces the thermal stress between the substrate and the upper coatings, and the refractory oxide as the top layer protects the underlayer coatings and the substrate from the corrosion of harsh environments [12–14]. The key requirements for selecting the top refractory oxides include good tolerance to harsh environments, thermal expansion match with the interlayer and the substrate materials, good phase stability at high temperatures, and low thermal conductivities. [12,15–17]. Particularly, cuspidine-type rare-earth aluminates $RE_4Al_2O_9$ are a class of ceramics that have been considered as potential materials for EBCs of silicon-based ceramics owing to their high melting point, low Young's modulus, good damage tolerance, close thermal expansion coefficients to that of mullite, low thermal conductivity, and good resistance to the hot gas atmosphere [15,18–21]. However, one major weakness of $RE_4Al_2O_9$ compounds for EBC application is the high-temperature phase transition with a sudden change in volume, which can lead to cracking of the coatings in thermal cycling [22–25]. Therefore, the suppression of phase transformation of $RE_4Al_2O_9$ compounds is of great significance for their high-temperature applications.

In recent years, a new type of ceramics consisting of multi-principal component elements in equal molar or near equal molar fractions but form single phase solid solutions have triggered much attention, which are referred to as high-entropy ceramics (HECs) [26–28]. These materials exhibit many intriguing properties, such as higher hardness, sluggish grain growth rate, lower thermal conductivity, strong microwave absorption capability, and better water-vapor resistance, etc. [29–34]. More importantly, our previous work indicates

that HECs usually possess better high-temperature phase stability than the single-component ceramics owing to the entropy stabilization effect of HECs [35,36], which may provide a new way to improve the phase stability of $RE_4Al_2O_9$ at high temperatures, i.e., through forming HE solid solutions. Consequently, to suppress high-temperature phase transformation and reduce the thermal conductivity of $RE_4Al_2O_9$ compounds, a novel HE cuspidine-structured rare-earth aluminate solid solution $(Nd_{0.2}Sm_{0.2}Eu_{0.2}Y_{0.2}Yb_{0.2})_4Al_2O_9$ was designed and successfully synthesized in this study. The phase composition, microstructure, phase stability, average linear thermal expansion coefficient, anisotropy of thermal expansion coefficient, and thermal conductivity of this new type of HE rare-earth aluminate were investigated synthetically. These fundamental data are of great importance to evaluate the prospect of $(Nd_{0.2}Sm_{0.2}Eu_{0.2}Y_{0.2}Yb_{0.2})_4Al_2O_9$ for EBC application. In addition, the mechanisms for low thermal conductivity and anisotropic thermal expansion will be presented.

2 Experimental

2.1 Synthesis of $(Nd_{0.2}Sm_{0.2}Eu_{0.2}Y_{0.2}Yb_{0.2})_4Al_2O_9$ powders

The starting materials used for synthesizing $(Nd_{0.2}Sm_{0.2}Eu_{0.2}Y_{0.2}Yb_{0.2})_4Al_2O_9$ powders are as follows: $RE(NO_3)_3 \cdot 6H_2O$ (RE = Nd, Sm, Eu, Y, and Yb) powders (99.9% purity, Aladdin Biochemical Technology Co., Ltd., Shanghai, China), $Al(NO_3)_3 \cdot 9H_2O$ powders (99.9% purity, Aladdin Biochemical Technology Co., Ltd., Shanghai, China), and ammonia ($NH_3 \cdot H_2O$, pH = 12.5, Beihua Fine Chem. Co., Ltd., Beijing, China).

A co-precipitation method was performed to synthesize $(Nd_{0.2}Sm_{0.2}Eu_{0.2}Y_{0.2}Yb_{0.2})_4Al_2O_9$ powders. Firstly, $RE(NO_3)_3 \cdot 6H_2O$ (RE = Nd, Sm, Eu, Y, and Yb) powders were weighted in equal molar ratio and mixed, then dissolved in distilled water to form a clear solution with a concentration of 0.3 mol/L. Separately, $Al(NO_3)_3 \cdot 9H_2O$ powders were also dissolved in distilled water to form a clear solution with the same molar concentration and then added into the mixed $RENO_3$ solution with stirring. The molar ratio of total RE elements and Al is RE_{total}:Al = 2:1. After mixing thoroughly, excess aqueous ammonia was added slowly into the mixed solution with vigorously stirring to obtain gel-like precipitants. The precipitants were

then filtered and washed with distilled water for several times to ensure impurity ions (NH_4^+ and NO_3^-) eliminated before being dried in an oven at 383 K for 12 h. Finally, the $(Nd_{0.2}Sm_{0.2}Eu_{0.2}Y_{0.2}Yb_{0.2})_4Al_2O_9$ powders were synthesized by calcining the precursors at 1873 K for 1 h in a muffle furnace. The calcined products were ball-milled with agate balls for 20 h by a planetary ball mill (XQM-2, NEWRICE Technology Co., Ltd.). The ball to powder weight ratio was controlled to be 6:1 and the speed of ball milling was 400 rpm. Then the mixed slurry was dried in a vacuum oven at room temperature. Fine-particle powders were obtained by screening the calcined products in a 300 mesh sieve.

2. 2   Preparation of bulk $(Nd_{0.2}Sm_{0.2}Eu_{0.2}Y_{0.2}Yb_{0.2})_4Al_2O_9$

Bulk $(Nd_{0.2}Sm_{0.2}Eu_{0.2}Y_{0.2}Yb_{0.2})_4Al_2O_9$ was prepared using a spark plasma sintering apparatus (SPS-20T-6-IV, Shanghai Chenhua Science and Technology Co., Ltd., China) at 1923 K for 4 min under a pressure of 30 MPa. Details of the preparation process were reported in our previous studies [31,32,36]. After sintering, the surface of the bulk sample was ground by silicon carbide sandpapers to remove the carburized layer.

2. 3   Characterization of $(Nd_{0.2}Sm_{0.2}Eu_{0.2}Y_{0.2}Yb_{0.2})_4Al_2O_9$ powders and the sintered compacts

The phase compositions of the as-synthesized powders and the sintered compacts were determined by an X-ray diffractometer (XRD, D8 Advanced, Bruker, Germany) using Cu Kα radiation ($\lambda = 1.5406$ Å) with a step size of 0.02°. The scanning rate was 2 (°)/min. The lattice parameters of as-synthesized $(Nd_{0.2}Sm_{0.2}Eu_{0.2}Y_{0.2}Yb_{0.2})_4Al_2O_9$ were refined by the Rietveld method (TOPAS, Bruker Corp., Karlsruhe, Germany).

The density of the sintered compacts was measured by Archimedes' method. The investigation of the microstructure and the element distributions of the sintered compacts were performed by using a scanning electron microscope (SEM, Apollo300, CamScan, Cambridge, UK) equipped with energy dispersive X-ray spectroscopic system (EDS, Inca X-Max 80T, Oxford, UK). Before the SEM observation, the samples were polished by silicon carbide sandpapers and then thermally etched at 1673 K for 2 h to ensure the grain boundary is clear.

The investigation of linear thermal expansion of $(Nd_{0.2}Sm_{0.2}Eu_{0.2}Y_{0.2}Yb_{0.2})_4Al_2O_9$ at 300–1473 K was performed by an optical dilatometer (Misura ODHT 1600-50, Expert System Solutions, Italy). The as-measured sample is a polished rectangular bar with a size of 3 mm × 4 mm × 15 mm. A 45° chamfer was cut at one end of the sample. The anisotropic thermal expansion coefficient of $(Nd_{0.2}Sm_{0.2}Eu_{0.2}Y_{0.2}Yb_{0.2})_4Al_2O_9$ was investigated by a powder X-ray diffractometer equipped with an isothermal sample heating system (XRD, X'Pert MPD Pro Panalytical Holland). $(Nd_{0.2}Sm_{0.2}Eu_{0.2}Y_{0.2}Yb_{0.2})_4Al_2O_9$ powders were heated from 300 to 1473 K at a heating rate of 5 K/min and held for 5 min to achieve temperature equilibration at 100 K intervals, and then the XRD patterns of the sample at the desired temperatures were recorded with a scanning rate of 1 (°)/min. The lattice parameters of $(Nd_{0.2}Sm_{0.2}Eu_{0.2}Y_{0.2}Yb_{0.2})_4Al_2O_9$ at different temperatures were refined by the Rietveld method. The volumetric thermal expansion coefficient (α_v) and the linear thermal expansion coefficients along principal axes (α_a, α_b, and α_c) were obtained by fitting the lattice parameters versus temperature curves of $(Nd_{0.2}Sm_{0.2}Eu_{0.2}Y_{0.2}Yb_{0.2})_4Al_2O_9$.

Thermal diffusivity of $(Nd_{0.2}Sm_{0.2}Eu_{0.2}Y_{0.2}Yb_{0.2})_4Al_2O_9$ was investigated by the laser flash method. The as-measured sample is a disk with a size of ϕ 10 mm × 2 mm. Before measurement, the surface of the sample was sprayed a layer of graphite to prevent heat radiation from penetrating through it. The heat capacity at constant pressure was calculated by Neumann–Kopp rule using the data of its constituent oxides (Nd_2O_3, Sm_2O_3, Eu_2O_3, Y_2O_3, Yb_2O_3, and Al_2O_3) [37,38]. Thermal conductivity (κ) was calculated by the following equation [39]:

$$\kappa = D_{th} \cdot C_p \cdot d \qquad (1)$$

where κ is thermal conductivity, D_{th} is thermal diffusivity, C_p is heat capacity at constant pressure, and d is bulk density of the sample.

3   Results and discussion

3. 1   Phase composition and microstructure

The first step for synthesizing HE rare-earth aluminate is choosing the compatible rare-earth elements that warrant the easy formation of phase-pure solid solution. Generally, there are two criteria for selecting the compatible components of HE materials [36]. Firstly, the difference in the ion radius of the selecting

elements is small. Secondly, the single-component phases containing the selected elements possess the same or similar crystal structures. Herein, the cation radius and radius difference of the selecting rare-earth elements for the design of HE rare-earth aluminate together with the space group of the single-component phases containing these rare-earth elements are listed in Table 1 [25]. It can be seen that the radius difference of the selected rare-earth elements is less than 13% and that all the single-component of $RE_4Al_2O_9$ (RE = Nd, Sm, Eu, Y, and Yb) possesses the same crystal structure, which warrants the easy formation of the phase-pure HE rare-earth aluminate. Figure 1 exhibits the crystal structure of rare-earth aluminate. The HE $(Nd_{0.2}Sm_{0.2}Eu_{0.2}Y_{0.2}Yb_{0.2})_4Al_2O_9$ has the same crystal structure with those of the single-component $RE_4Al_2O_9$, which crystallizes in a monoclinic structure with a space group of $P2_1/c$ and five component elements (Nd, Sm, Eu, Y, and Yb) occupy the RE sites evenly and randomly [40].

Figure 2 shows the XRD pattern of as-synthesized $(Nd_{0.2}Sm_{0.2}Eu_{0.2}Y_{0.2}Yb_{0.2})_4Al_2O_9$ powders, and the data of single-component $RE_4Al_2O_9$ (RE = Nd, Sm, Eu, Y, and Yb) obtained from ICDD/JCPDS cards are also exhibited for comparison. The as-synthesized powders are phase-pure and only a monoclinic phase was detected, indicating that a solid solution $(Nd_{0.2}Sm_{0.2}Eu_{0.2}Y_{0.2}Yb_{0.2})_4Al_2O_9$ is formed. Rietveld refinement was performed by using TOPAS software to obtain information about the lattice parameters of $(Nd_{0.2}Sm_{0.2}Eu_{0.2}Y_{0.2}Yb_{0.2})_4Al_2O_9$. The results are presented in Table 2 and compared with the data of the single-component $RE_4Al_2O_9$ (RE = Nd, Sm, Eu, Y, and Yb) obtained from ICDD/JCPDS cards. It can be seen that the refined lattice parameters (*a*, *b*, and *c*) of
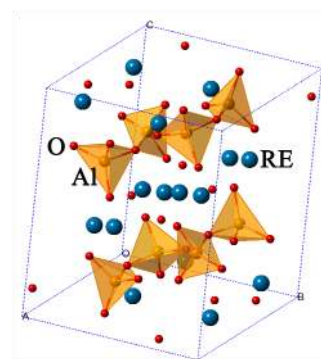

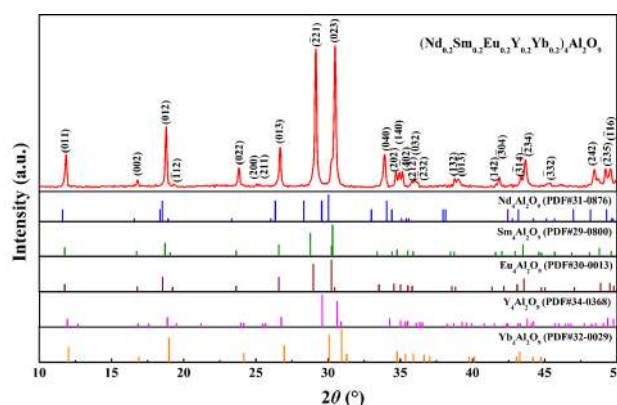**Fig. 1** Crystal structure of rare-earth aluminate.

Fig. 2 XRD patterns of the as-synthesized $(Nd_{0.2}Sm_{0.2}Eu_{0.2}Y_{0.2}Yb_{0.2})_4Al_2O_9$ powders together with the data of single-component $RE_4Al_2O_9$ (RE = Nd, Sm, Eu, Y, and Yb) obtained from ICDD/JCPDS cards.

Table 1 Space group, cation radius, and radius difference of $RE_4Al_2O_9$ for design of HE rare-earth aluminates (the data are obtained from the database of Materials Studio program, © Accelrys Inc., San Diego, USA, 2014)

Phase	Space group	Rare-earth element	Cation radius (Å)	Radius difference (%)
$RE_4Al_2O_9$	$P2_1/c$	Nd	0.98	12.64
		Sm	0.96	10.34
		Eu	0.95	9.20
		Y	0.90	3.45
		Yb	0.87	0

Table 2 Refined lattice parameters, relative change of lattice parameters compared to $Yb_4Al_2O_9$, and theoretical density of HE $(Nd_{0.2}Sm_{0.2}Eu_{0.2}Y_{0.2}Yb_{0.2})_4Al_2O_9$ together with those of the single-component $RE_4Al_2O_9$ (RE = Nd, Sm, Eu, Y, and Yb) obtained from ICDD/JCPDS cards

Phase	*a* (Å)	*b* (Å)	*c* (Å)	$\Delta a/a_{Yb}$ (%)	$\Delta b/b_{Yb}$ (%)	$\Delta c/c_{Yb}$ (%)	β (°)	*d* (g/cm³)
HE $RE_4Al_2O_9$	7.511	10.573	11.172	3.20	2.55	1.20	109.1	6.06
$Nd_4Al_2O_9$	7.725	10.846	11.306	6.14	5.20	2.41	109.3	6.63
$Sm_4Al_2O_9$	7.520	10.700	11.190	3.33	3.78	1.36	108.9	6.99
$Eu_4Al_2O_9$	7.533	10.696	11.180	3.50	3.74	1.27	108.8	6.76
$Y_4Al_2O_9$	7.379	10.469	11.116	1.39	1.54	0.69	108.6	5.28
$Yb_4Al_2O_9$	7.278	10.310	11.040	0	0	0	108.3	8.30

$(Nd_{0.2}Sm_{0.2}Eu_{0.2}Y_{0.2}Yb_{0.2})_4Al_2O_9$ are larger than those of $Y_4Al_2O_9$ and $Yb_4Al_2O_9$ but smaller than those of $Nd_4Al_2O_9$, $Sm_4Al_2O_9$, and $Eu_4Al_2O_9$. Based on the refined lattice parameters, the theoretical density of $(Nd_{0.2}Sm_{0.2}Eu_{0.2}Y_{0.2}Yb_{0.2})_4Al_2O_9$ is calculated to be 6.06 g/cm^3, which is between the data of five single-component phases.

Figure 3 illustrates the XRD pattern of the as-sintered $(Nd_{0.2}Sm_{0.2}Eu_{0.2}Y_{0.2}Yb_{0.2})_4Al_2O_9$ compact. The phase composition of the as-sintered compact is unchanged compared with that of the as-synthesized powders. Figure 4 displays the SEM image of the as-sintered $(Nd_{0.2}Sm_{0.2}Eu_{0.2}Y_{0.2}Yb_{0.2})_4Al_2O_9$ compact after thermally etched at 1673 K for 2 h and the corresponding EDS mappings of rare-earth elements (Nd, Sm, Eu, Y, and Yb). No pores and cracks can be found from the observed region, indicating that the as-sintered compact has a high relative density. The experimental density of the as-sintered compact measured by the Archimedes' method is 6.02 g/cm^3 and the corresponding relative density is 99%. It also can be found that the containing rare-earth elements are uniformly distributed in the grains, which further indicate that $(Nd_{0.2}Sm_{0.2}Eu_{0.2}Y_{0.2}Yb_{0.2})_4Al_2O_9$ is a single-phase solid solution.

3. 2 Phase stability and thermal expansion behavior

The linear thermal expansion curve of $(Nd_{0.2}Sm_{0.2}Eu_{0.2}Y_{0.2}Yb_{0.2})_4Al_2O_9$ measured at 300–1473 K is illustrated in Fig. 5. It is evident that the expansion of bulk $(Nd_{0.2}Sm_{0.2}Eu_{0.2}Y_{0.2}Yb_{0.2})_4Al_2O_9$ increases linearly with the increase of temperature and no abrupt volume change was found, which indicates
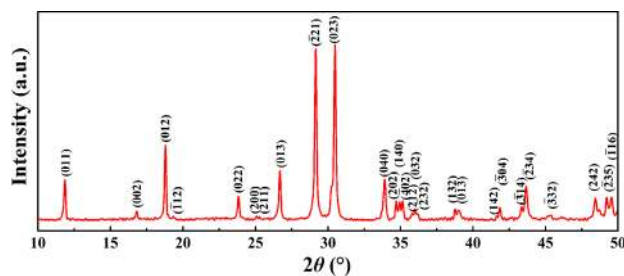
Fig. 3 XRD pattern of the as-sintered $(Nd_{0.2}Sm_{0.2}Eu_{0.2}Y_{0.2}Yb_{0.2})_4Al_2O_9$ compact.

that $(Nd_{0.2}Sm_{0.2}Eu_{0.2}Y_{0.2}Yb_{0.2})_4Al_2O_9$ has good phase stability at the measured temperature range. Note that the single-component $Sm_4Al_2O_9$ and $Eu_4Al_2O_9$ exhibit reversible phase transition with abrupt volume changes at 1317 and 1387 K, respectively [25]. This phase transition is harmful to the materials applied in the high-temperature environment due to that the sudden change in volume will reduce the thermal shock resistance of the materials and cause the cracking of coatings in thermal cycling. Thus, good phase stability of high-entropy $(Nd_{0.2}Sm_{0.2}Eu_{0.2}Y_{0.2}Yb_{0.2})_4Al_2O_9$ renders it more suitable for high-temperature applications.

In addition, the thermal expansion versus temperature curve in Fig. 5 can be fitted using a linear function: $\Delta L/L_0 \times 100\% = 6.96\times10^{-6}T(K) - 0.25$, with a reliability value of $R^2 = 0.999$. The linear thermal expansion coefficient of $(Nd_{0.2}Sm_{0.2}Eu_{0.2}Y_{0.2}Yb_{0.2})_4Al_2O_9$ is determined in terms of the slope of the curve and calculated to be 6.96×10^{-6} K^{-1} at 300–1473 K, which is in between those of $Y_4Al_2O_9$ (7.37×10^{-6} K^{-1}) [19] and $Yb_4Al_2O_9$ (6.27×10^{-6} K^{-1}) [16], and close to that of the interlayer phase of EBC system, mullite (5×10^{-6}–7×10^{-6} K^{-1}) [41].
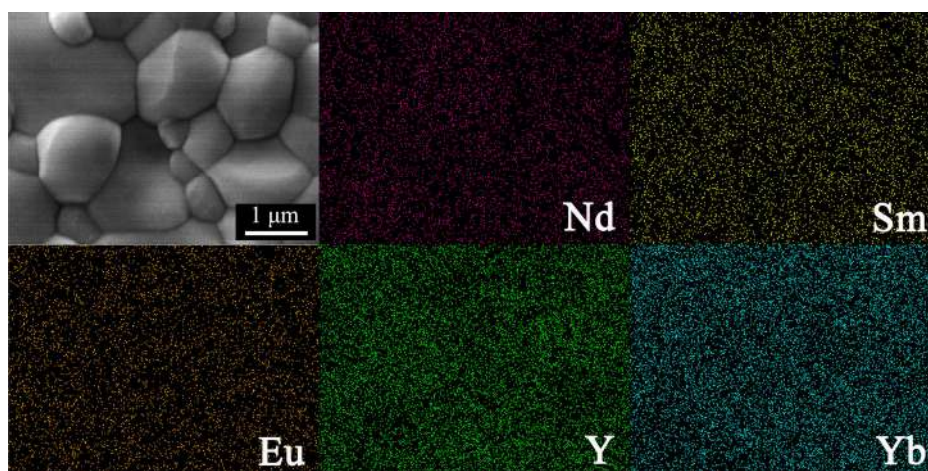
Fig. 4 SEM image of the as-sintered $(Nd_{0.2}Sm_{0.2}Eu_{0.2}Y_{0.2}Yb_{0.2})_4Al_2O_9$ compact after thermally etched at 1673 K for 2 h and the corresponding EDS mappings of rare-earth elements (Nd, Sm, Eu, Y, and Yb).
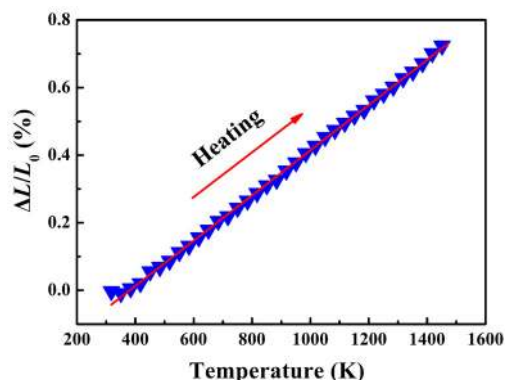
Fig. 5 Linear thermal expansion curve of $(Nd_{0.2}Sm_{0.2}Eu_{0.2}Y_{0.2}Yb_{0.2})_4Al_2O_9$ measured at 300–1473 K.

To investigate the anisotropy of the thermal expansion of $(Nd_{0.2}Sm_{0.2}Eu_{0.2}Y_{0.2}Yb_{0.2})_4Al_2O_9$, the XRD patterns of $(Nd_{0.2}Sm_{0.2}Eu_{0.2}Y_{0.2}Yb_{0.2})_4Al_2O_9$ powders at different temperatures were recorded and are exhibited in Fig. 6. It can be seen that there is no phase transformation detected when the temperature increases from 300 to 1473 K, further proving that $(Nd_{0.2}Sm_{0.2}Eu_{0.2}Y_{0.2}Yb_{0.2})_4Al_2O_9$ has good phase stability at high temperatures. The diffraction peaks of $(Nd_{0.2}Sm_{0.2}Eu_{0.2}Y_{0.2}Yb_{0.2})_4Al_2O_9$ gradually shift to the lower angle direction with the increase of temperature, which indicates that the lattice parameters of $(Nd_{0.2}Sm_{0.2}Eu_{0.2}Y_{0.2}Yb_{0.2})_4Al_2O_9$ change when the temperature increases. The lattice parameters of $(Nd_{0.2}Sm_{0.2}Eu_{0.2}Y_{0.2}Yb_{0.2})_4Al_2O_9$ at different temperatures were obtained by fitting the XRD patterns in Fig. 6 according to the Rietveld refinement method.

Figure 7 shows the normalized lattice parameters of $(Nd_{0.2}Sm_{0.2}Eu_{0.2}Y_{0.2}Yb_{0.2})_4Al_2O_9$ at 300–1473 K. The lattice parameters a, b, c, and the unit cell volume V monotonously increase as the temperature increases from 300 to 1473 K. The α_v, namely, the relative change in volume when the temperature rises by 1 K, is defined by the following equations [42]:

$$\alpha_v = \frac{1}{V}\left(\frac{\partial V}{\partial T}\right) \quad \text{or} \quad V(T) = V_0 \exp\left[\int \alpha_v(T)dT\right] \quad (2)$$

where $\alpha_v(T)$ is the temperature-dependent volumetric thermal expansion coefficient, V_0 is the volume of a unit cell at 300 K. $\alpha_v(T)$ tends to be a constant at high temperatures and thus Eq. (2) can be simplified as

$$\ln(V/V_0) = \alpha_v(T - T_0) \quad (3)$$

Based on Eq. (3), the α_v of $(Nd_{0.2}Sm_{0.2}Eu_{0.2}Y_{0.2}Yb_{0.2})_4Al_2O_9$ can be obtained by fitting the data in Fig. 7. Moreover, the linear thermal expansion coefficients along three

crystallographic directions (α_a, α_b, and α_c) were also calculated in the same way. Table 3 shows the anisotropic thermal expansion coefficients (α_a, α_b, and α_c) and α_v of $(Nd_{0.2}Sm_{0.2}Eu_{0.2}Y_{0.2}Yb_{0.2})_4Al_2O_9$ together with those of $Y_4Al_2O_9$ [19]. The α_v of $(Nd_{0.2}Sm_{0.2}Eu_{0.2}Y_{0.2}Yb_{0.2})_4Al_2O_9$ $(24.40\times10^{-6}\ K^{-1})$ is slightly higher than that of $Y_4Al_2O_9$ $(23.37\times10^{-6}\ K^{-1})$, and the anisotropy of thermal expansion coefficients of $(Nd_{0.2}Sm_{0.2}Eu_{0.2}Y_{0.2}Yb_{0.2})_4Al_2O_9$ is much stronger than that of $Y_4Al_2O_9$.

To obtain an intuitive and complete representation of the anisotropic thermal expansion coefficients of $(Nd_{0.2}Sm_{0.2}Eu_{0.2}Y_{0.2}Yb_{0.2})_4Al_2O_9$, the variation of thermal
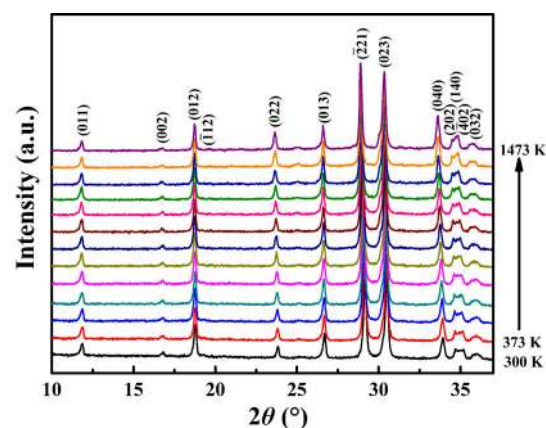
Fig. 6 XRD patterns of $(Nd_{0.2}Sm_{0.2}Eu_{0.2}Y_{0.2}Yb_{0.2})_4Al_2O_9$ powders at different temperatures.
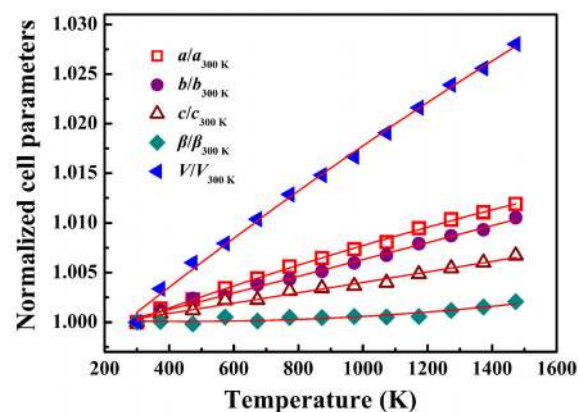
Fig. 7 Normalized lattice parameters of $(Nd_{0.2}Sm_{0.2}Eu_{0.2}Y_{0.2}Yb_{0.2})_4Al_2O_9$ at 300–1473 K.

Table 3 Anisotropic thermal expansion coefficients (α_a, α_b, and α_c) and α_v of $(Nd_{0.2}Sm_{0.2}Eu_{0.2}Y_{0.2}Yb_{0.2})_4Al_2O_9$ together with those of $Y_4Al_2O_9$

Compounds	α_a ($10^{-6}\ K^{-1}$)	α_b ($10^{-6}\ K^{-1}$)	α_c ($10^{-6}\ K^{-1}$)	α_v ($10^{-6}\ K^{-1}$)
HE $RE_4Al_2O_9$	10.59	8.93	5.66	24.40
$Y_4Al_2O_9$	7.34	7.54	7.61	23.37

expansion coefficients as a function of crystal orientation is necessary. Figure 8 exhibits the surface contour of the thermal expansion coefficients of $(Nd_{0.2}Sm_{0.2}Eu_{0.2}Y_{0.2}Yb_{0.2})_4Al_2O_9$ and the planar projections of the thermal expansion coefficients on (001), (010), and (100) crystallographic planes. It can be seen that the anisotropy of thermal expansion coefficients of $(Nd_{0.2}Sm_{0.2}Eu_{0.2}Y_{0.2}Yb_{0.2})_4Al_2O_9$ is clearly illustrated and the anisotropy of thermal expansion coefficients on (010) plane is stronger than those on (001) and (100) planes. The maximum and minimum values of thermal expansion coefficients are $10.60 \times 10^{-6} K^{-1}$ (α_{11}) and $4.87 \times 10^{-6} K^{-1}$ (α_{33}), respectively. The strong anisotropy of thermal expansion coefficients of $(Nd_{0.2}Sm_{0.2}Eu_{0.2}Y_{0.2}Yb_{0.2})_4Al_2O_9$ can be explained by the crystal structure feature of $RE_4Al_2O_9$. Figure 9 exhibits the planar projections of the crystal structure of $(Nd_{0.2}Sm_{0.2}Eu_{0.2}Y_{0.2}Yb_{0.2})_4Al_2O_9$ on (001), (010), and (100) crystallographic planes. It can be seen that the arrangement of RE atoms along a- and b-axis is much denser than that along the c-axis. Thus, the fluctuation of the lattice parameters a and b is much stronger than that of the lattice parameter c when the RE^{3+} radius changes, which is demonstrated by the relative change regularity of the lattice parameters of $RE_4Al_2O_9$ compounds. Figure 10 shows the relative change of the lattice parameters of $RE_4Al_2O_9$ (RE = Nd, Sm, Eu, Y, and Yb) as a function of RE^{3+} radius, and the data were obtained from ICDD/JCPDS cards and are
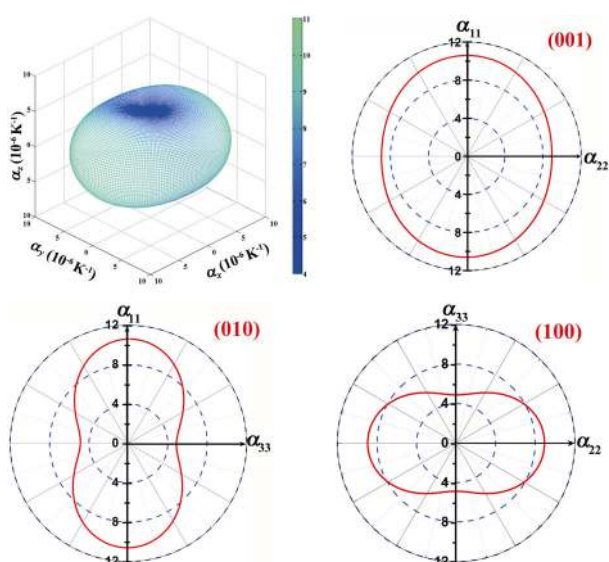
listed in Table 2. As the RE^{3+} radius increases, the relative change of the lattice parameters a and b are much larger than that of the lattice parameter c, which will result in the anisotropy of bonding strength, i.e., the bonds along a- and b-axis are weaker than that along the c-axis.

Quantitative description of this bonding anisotropy is accessible by estimating the bond energy of HE $RE_4Al_2O_9$ and $Y_4Al_2O_9$ using a simple theory called chemical bonding theory (CBT). Due to the similarity in the crystal structure, the calculation procedure for
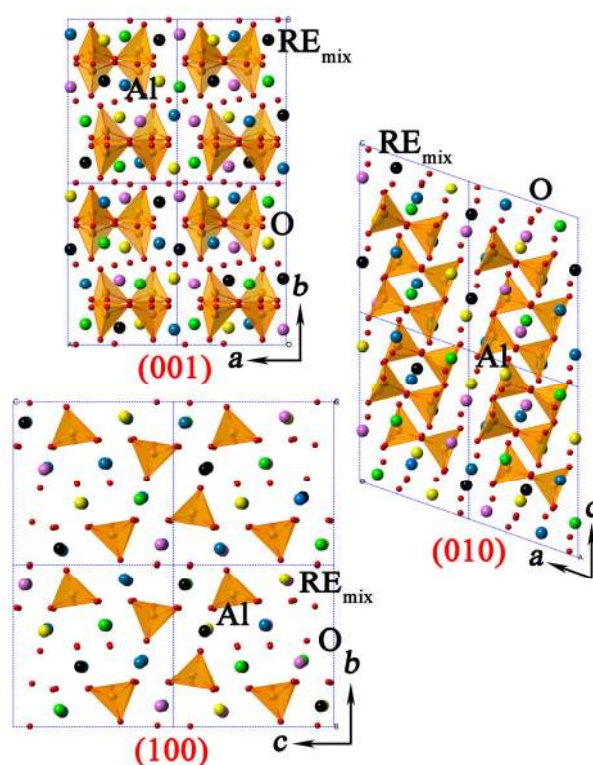
Fig. 9 Planar projections of the crystal structure of $(Nd_{0.2}Sm_{0.2}Eu_{0.2}Y_{0.2}Yb_{0.2})_4Al_2O_9$ on (001), (010), and (100) crystallographic planes.

Fig. 8 Surface contour of the thermal expansion coefficients of $(Nd_{0.2}Sm_{0.2}Eu_{0.2}Y_{0.2}Yb_{0.2})_4Al_2O_9$ and planar projections of the thermal expansion coefficients on (001), (010), and (100) crystallographic planes.

Fig. 10 Relative change of the lattice parameters of $RE_4Al_2O_9$ (RE = Nd, Sm, Eu, Y, and Yb) as a function of RE^{3+} radius.

parameters of all chemical bonds in HE $(Nd_{0.2}Sm_{0.2}Eu_{0.2}Y_{0.2}Yb_{0.2})_4Al_2O_9$ is the same as that in $Y_4Al_2O_9$, and for detail description, one may refer to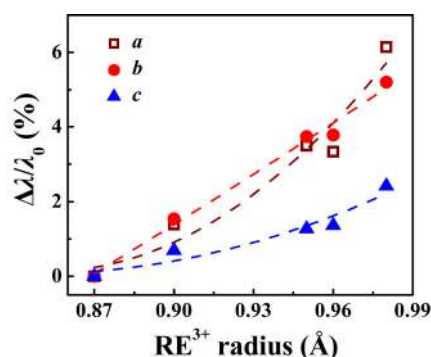 Ref. [18]. The chemical parameters for each bond of two materials are listed in Table 4 (worth noting that the listed bond energies for HE $(Nd_{0.2}Sm_{0.2}Eu_{0.2}Y_{0.2}Yb_{0.2})_4Al_2O_9$ are the average ones since the bond length (l^μ) around different rare-earth atoms is different. For both materials, the covalency (f_c^μ) and bond energies (U^μ) of Al–O bonds are significantly larger than those of RE–O bonds, demonstrating stronger bonding nature of Al–O tetrahedron. Large bond energy also leads to less contribution of AlO_4 tetrahedron to total thermal expansion, and the chemical environments around RE atoms determine the expansion behavior of HE $(Nd_{0.2}Sm_{0.2}Eu_{0.2}Y_{0.2}Yb_{0.2})_4Al_2O_9$. With different RE atoms incorporating in the structure, the bond strength of all RE–O bonds varies accordingly. However, the energy changing for different RE–O bonds is quite anisotropic, e.g., the response of RE1–O3, RE1–O7, RE1–O2, and RE1–O1 is more evident than the rest RE1–O bonds. The spatial configuration of RE1–O polyhedra is shown in Fig. 11(a). The bonds with large energy degradation are almost parallel with *ab*-plane, leading to an increase of anisotropy in bonding strength

between the *ab*-plane and *c*-direction. For the other three RE sites listed in Table 4, the same situation is observed, and the RE–O bonds along the *ab*-plane are disturbed notably than that along the *c*-direction. Since the thermal expansion of $RE_4Al_2O_9$ is determined by RE–O bonds, the increase of anisotropy of RE–O bonds along different directions will eventually result in the increase of anisotropy in thermal expansion. In addition, the same variety trend was also found from Young's modulus of $RE_4Al_2O_9$ compounds. The anisotropy of Young's modulus of $Yb_4Al_2O_9$ is weaker than that of $Y_4Al_2O_9$ due to that Yb^{3+} has a smaller radius than Y^{3+}, which also proves that $RE_4Al_2O_9$ with large RE^{3+} radius exhibits the strong anisotropy of bonding strength [16,18].

3.3 Thermal conductivity

Table 5 shows the thermal diffusivity, heat capacity, bulk density, and thermal conductivity of $(Nd_{0.2}Sm_{0.2}Eu_{0.2}Y_{0.2}Yb_{0.2})_4Al_2O_9$ measured at room temperature. The thermal conductivity of $(Nd_{0.2}Sm_{0.2}Eu_{0.2}Y_{0.2}Yb_{0.2})_4Al_2O_9$ at room temperature is as low as 1.50 $W \cdot m^{-1} \cdot K^{-1}$, which is 55% lower than that of $Y_4Al_2O_9$ (3.31 $W \cdot m^{-1} \cdot K^{-1}$). This value is also much lower than those of other candidate EBC materials,

Table 4 Chemical parameters of each bond for $(Nd_{0.2}Sm_{0.2}Eu_{0.2}Y_{0.2}Yb_{0.2})_4Al_2O_9$ and $Y_4Al_2O_9$ by chemical bond theory

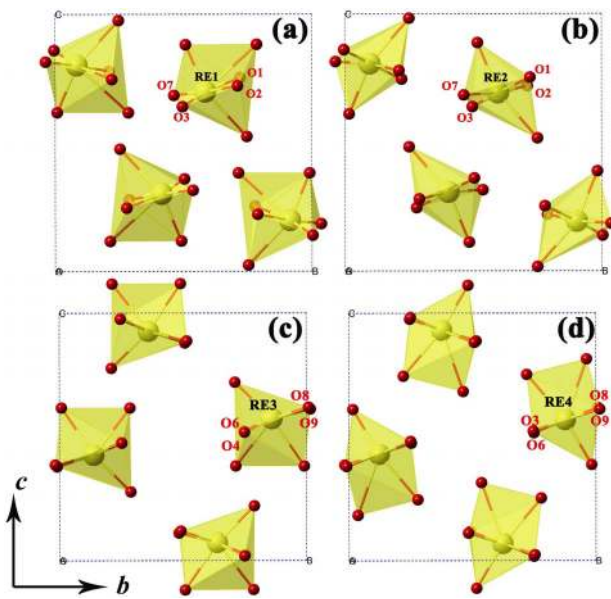| Bond	$Y_4Al_2O_9$			$(Nd_{0.2}Sm_{0.2}Eu_{0.2}Y_{0.2}Yb_{0.2})_4Al_2O$			Bond	$Y_4Al_2O_9$			$(Nd_{0.2}Sm_{0.2}Eu_{0.2}Y_{0.2}Yb_{0.2})_4Al_2O$		
	l^μ (Å)	f_c^μ	U^μ (kJ·mol⁻¹)	l^μ (Å)	f_c^μ	U^μ (kJ·mol⁻¹)		l^μ (Å)	f_c^μ	U^μ (kJ·mol⁻¹)	l^μ (Å)	f_c^μ	U^μ (kJ·mol⁻¹)
RE1–O3	2.0622	0.12	930	2.0931	0.13	919	RE3–O6	2.5893	0.12	844	2.6255	0.12	835
RE1–O8	2.0917	0.12	999	2.0967	0.13	997	RE3–O9	2.7703	0.11	799	2.8103	0.12	789
RE1–O7	2.2460	0.22	950	2.2778	0.22	940	RE4–O3	2.1601	0.12	974	2.1866	0.12	965
RE1–O2	2.3991	0.12	897	2.4330	0.12	887	RE4–O6	2.2073	0.12	958	2.2223	0.12	948
RE1–O6	2.5124	0.12	865	2.5247	0.12	862	RE4–O9	2.2141	0.12	956	2.2381	0.12	953
RE1–O1	2.6015	0.12	841	2.6395	0.12	831	RE4–O9	2.2888	0.12	931	2.3177	0.12	922
RE1–O5	2.8560	0.11	779	2.8723	0.12	775	RE4–O8	2.4787	0.12	874	2.5148	0.12	864
RE2–O2	1.9238	0.18	1306	1.9509	0.18	1292	RE4–O1	2.5418	0.12	857	2.5544	0.12	853
RE2–O3	2.1103	0.16	1116	2.1377	0.16	1105	RE4–O7	2.7460	0.11	804	2.7523	0.12	803
RE2–O9	2.2430	0.17	1162	2.2482	0.17	1160	Al1–O4	1.7267	0.57	2297	1.7314	0.58	2290
RE2–O1	2.3228	0.29	1130	2.3519	0.29	1119	Al1–O3	1.8286	0.35	2097	1.8457	0.35	2082
RE2–O4	2.4799	0.16	1074	2.4936	0.16	1069	Al1–O5	1.8338	0.39	2275	1.8644	0.39	2246
RE2–O7	2.5044	0.16	1065	2.5410	0.16	1053	Al1–O2	1.9883	0.38	2146	1.9975	0.38	2136
RE3–O8	2.1966	0.12	962	2.2225	0.12	953	Al2–O6	1.5632	0.41	2539	1.5703	0.41	2529
RE3–O2	2.2160	0.12	955	2.2279	0.12	951	Al2–O5	1.6917	0.40	2407	1.7201	0.40	2377
RE3–O4	2.2762	0.12	935	2.3098	0.12	925	Al2–O7	1.7978	0.39	2307	1.8114	0.39	2292
RE3–O8	2.4375	0.12	886	2.4467	0.12	884	Al2–O1	1.8279	0.39	2280	1.8348	0.39	2272
RE3–O5	2.5367	0.12	858	2.5473	0.12	855	—	—	—	—	—	—	—

Fig. 11 Spatial configuration of RE–O polyhedra for (a) RE1, (b) RE2, (c) RE3, and (d) RE4 sites, respectively.

Table 5 Thermal diffusivity (D_{th}), heat capacity (C_p), bulk density (d), and thermal conductivity (κ) of $(Nd_{0.2}Sm_{0.2}Eu_{0.2}Y_{0.2}Yb_{0.2})_4Al_2O_9$ measured at room temperature

D_{th} (mm²/s)	C_p (J·mol⁻¹·K⁻¹)	d (g/cm³)	κ (W·m⁻¹·K⁻¹)
0.62	306.92	6.02	1.50

such as Y_2SiO_5 (1.86 W·m⁻¹·K⁻¹) [43], Yb_2SiO_5 (2.3 W·m⁻¹·K⁻¹) [44], γ-$Y_2Si_2O_7$ (4.91 W·m⁻¹·K⁻¹) [43], and β-$Yb_2Si_2O_7$ (4.31 W·m⁻¹·K⁻¹) [45]. The low thermal conductivity of $(Nd_{0.2}Sm_{0.2}Eu_{0.2}Y_{0.2}Yb_{0.2})_4Al_2O_9$ is likely attributed to the HE effect [28]. For opaque dielectric materials, the major process that leads to a finite thermal conductivity is phonon scattering and the extent of phonon scattering depends on the anharmonicity of the lattice vibrations [46]. Based on the Umklapp phonon–phonon scattering mechanism [47,48]:

$$\kappa_a = \frac{(6\pi^2)^{2/3}}{4\pi^2} \frac{\overline{M}v_s^3}{TV_a^{2/3}\gamma^2}\left(\frac{1}{N^{1/3}}\right) \qquad (4)$$

where κ_a is the thermal conductivity of acoustic contribution, $\overline{M}$ is average mass, v_s is average speed of sound, T is temperature, V_a is the volume per atom, γ is Grüneisen parameter, and N is atom per primitive cell. For $(Nd_{0.2}Sm_{0.2}Eu_{0.2}Y_{0.2}Yb_{0.2})_4Al_2O_9$, five rare-earth atoms with different atomic mass and bonding strengths share RE-site in the crystal structure, resulting in increased structural complexity. Correspondingly, the number of N of $(Nd_{0.2}Sm_{0.2}Eu_{0.2}Y_{0.2}Yb_{0.2})_4Al_2O_9$ increases and its thermal conductivity decreases. Point

defect scattering is also a dominant process that giving rise to the low thermal conductivity of HE materials. Based on the point defect scattering mechanism [49,50]:

$$\kappa_L = \frac{1}{3}\int_0^{\omega_{max}} C_s(\omega)v_g(\omega)^2\tau(\omega)d\omega \qquad (5)$$

$$\tau_{PD}^{-1} = \frac{V\omega^4}{4\pi v_p^2 v_g}\left[\sum_i f_i\left(1-\frac{m_i}{\overline{m}}\right)^2 + \sum_i f_i\left(1-\frac{r_i}{\overline{r}}\right)^2\right] \qquad (6)$$

where κ_L is lattice thermal conductivity, $C_s(\omega)$ is spectral heat capacity, τ is phonon relaxation time, ω is phonon frequency, v_p is phonon phase velocity, v_g is phonon group velocity, f_i is the fraction of atoms with mass m_i and radius r_i that reside on a site with average mass and radius ($\overline{m}$ and $\overline{r}$), respectively. It can be found from Eqs. (5) and (6) that scattering by point defect arises from the fluctuations of mass and strain within the lattice. For $(Nd_{0.2}Sm_{0.2}Eu_{0.2}Y_{0.2}Yb_{0.2})_4Al_2O_9$, the severe lattice distortion caused by the HE effect will result in the increase of the fluctuations of mass and strain within the lattice [51]. This can lead to the intensification of phonon scattering and decrease of the thermal conductivity of $(Nd_{0.2}Sm_{0.2}Eu_{0.2}Y_{0.2}Yb_{0.2})_4Al_2O_9$.

For a desirable EBC material, possessing good phase stability from room temperature to the service temperature is essential. Meanwhile, thermal expansion matches those of the substrate and the interlayer is also required to minimize the thermal stress and ensure that the coating does not crack in thermal cycling. The investigation on the thermal properties of $(Nd_{0.2}Sm_{0.2}Eu_{0.2}Y_{0.2}Yb_{0.2})_4Al_2O_9$ in this study ascertains that $(Nd_{0.2}Sm_{0.2}Eu_{0.2}Y_{0.2}Yb_{0.2})_4Al_2O_9$ exhibits good phase stability at high temperatures, close thermal expansion coefficient to that of the interlayer mullite, and extremely low thermal conductivity. These results indicate that $(Nd_{0.2}Sm_{0.2}Eu_{0.2}Y_{0.2}Yb_{0.2})_4Al_2O_9$ is a promising candidate EBC material of silicon-based structural ceramics.

4 Conclusions

In this study, a novel HE cuspidine-structured rare-earth aluminate ceramic $(Nd_{0.2}Sm_{0.2}Eu_{0.2}Y_{0.2}Yb_{0.2})_4Al_2O_9$ was designed and successfully synthesized. The investigation of the phase composition and the micro structure proves that the synthesized $(Nd_{0.2}Sm_{0.2}Eu_{0.2}Y_{0.2}Yb_{0.2})_4Al_2O_9$ is a phase-pure solid solution with uniform component

distribution. $(Nd_{0.2}Sm_{0.2}Eu_{0.2}Y_{0.2}Yb_{0.2})_4Al_2O_9$ exhibits good high-temperature phase stability and no phase transition is detected from 300 to 1473 K. The linear thermal expansion coefficient of $(Nd_{0.2}Sm_{0.2}Eu_{0.2}Y_{0.2}Yb_{0.2})_4Al_2O_9$ at 300–1473 K is $6.96\times10^{-6}\,K^{-1}$, which is close to that of the interlayer mullite of EBC system. The anisotropy of thermal expansion coefficient of $(Nd_{0.2}Sm_{0.2}Eu_{0.2}Y_{0.2}Yb_{0.2})_4Al_2O_9$ is stronger than that of $Y_4Al_2O_9$ due to the anisotropy of bonding strength of $(Nd_{0.2}Sm_{0.2}Eu_{0.2}Y_{0.2}Yb_{0.2})_4Al_2O_9$. The volumetric thermal expansion coefficient and the anisotropic thermal expansion coefficients of $(Nd_{0.2}Sm_{0.2}Eu_{0.2}Y_{0.2}Yb_{0.2})_4Al_2O_9$ are: $\alpha_v = 24.40\times10^{-6}\,K^{-1}$, $\alpha_a = 10.59\times10^{-6}\,K^{-1}$, $\alpha_b = 8.93\times10^{-6}\,K^{-1}$, and $\alpha_c = 5.66\times10^{-6}\,K^{-1}$. $(Nd_{0.2}Sm_{0.2}Eu_{0.2}Y_{0.2}Yb_{0.2})_4Al_2O_9$ exhibits low thermal conductivity owing to the intensification of phonon scattering caused by HE effect. The thermal conductivity of $(Nd_{0.2}Sm_{0.2}Eu_{0.2}Y_{0.2}Yb_{0.2})_4Al_2O_9$ at room temperature is $1.50\ W\cdot m^{-1}\cdot K^{-1}$, which is 55% lower than that of $Y_4Al_2O_9$. Good high-temperature phase stability, close thermal expansion coefficient to that of the interlayer mullite, and extremely low thermal conductivity of $(Nd_{0.2}Sm_{0.2}Eu_{0.2}Y_{0.2}Yb_{0.2})_4Al_2O_9$ make this material promising as a candidate EBC material of silicon-based structural ceramics.

Acknowledgements

References

[1] Klemm H. Silicon nitride for high-temperature applications. *J Am Ceram Soc* 2010, **93**: 1501–1522.

[2] Naslain R, Christin F. SiC-matrix composite materials for advanced jet engines. *MRS Bull* 2003, **28**: 654–658.

[3] Naslain R. Design, preparation and properties of non-oxide CMCs for application in engines and nuclear reactors: An overview. *Compos Sci Technol* 2004, **64**: 155–170.

[4] Becher PF, Hsueh CH, Angelini P, *et al*. Toughening behavior in whisker-reinforced ceramic matrix composites. *J Am Ceram Soc* 1988, **71**: 1050–1061.

[5] Igawa N, Taguchi T, Nozawa T, *et al*. Fabrication of SiC fiber reinforced SiC composite by chemical vapor infiltration for excellent mechanical properties. *J Phys Chem Solids* 2005, **66**: 551–554.

[6] Jacobson NS. Corrosion of silicon-based ceramics in combustion environments. *J Am Ceram Soc* 1993, **76**: 3–28.

[7] Smialek JL, Robinson RC, Opila EJ, *et al*. SiC and Si₃N₄ recession due to SiO₂ scale volatility under combustor conditions. *Adv Compos Mater* 1999, **8**: 33–45.

[8] Klemm H, Taut C, Wötting G. Long-term stability of nonoxide ceramics in an oxidative environment at 1500 ℃. *J Eur Ceram Soc* 2003, **23**: 619–627.

[9] Tortorelli PF, More KL. Effects of high water-vapor pressure on oxidation of silicon carbide at 1200 ℃. *J Am Ceram Soc* 2003, **86**: 1249–1255.

[10] More KL, Tortorelli PF, Walker LR, *et al*. High-temperature stability of SiC-based composites in high-water-vapor-pressure environments. *J Am Ceram Soc* 2003, **86**: 1272–1281.

[11] Opila EJ. Oxidation and volatilization of silica formers in water vapor. *J Am Ceram Soc* 2003, **86**: 1238–1248.

[12] Lee KN. Current status of environmental barrier coatings for Si-based ceramics. *Surf Coat Technol* 2000, **133–134**: 1–7.

[13] Lee KN, Fox DS, Bansal NP. Rare earth silicate environmental barrier coatings for SiC/SiC composites and Si3N4 ceramics. *J Eur Ceram Soc* 2005, **25**: 1705–1715.

[14] Richards BT, Wadley HNG. Plasma spray deposition of tri-layer environmental barrier coatings. *J Eur Ceram Soc* 2014, **34**: 3069–3083.

[15] Lee KN, Miller RA. Development and environmental durability of mullite and mullite/YSZ dual layer coatings for SiC and Si₃N₄ ceramics. *Surf Coat Technol* 1996, **86**: 142–148.

[16] Xiang HM, Feng ZH, Li ZP, *et al*. Crystal structure, mechanical and thermal properties of Yb₄Al₂O₉: A combination of experimental and theoretical investigations. *J Eur Ceram Soc* 2017, **37**: 2491–2499.

[17] Lee KN, Miller RA, Jacobson NS. New generation of plasma-sprayed mullite coatings on silicon carbide. *J Am Ceram Soc* 1995, **78**: 705–710.

[18] Zhou YC, Xiang HM, Lu XP, *et al*. Theoretical prediction on mechanical and thermal properties of a promising thermal barrier material: Y₄Al₂O₉. *J Adv Ceram* 2015, **4**: 83–93.

[19] Zhou YC, Lu XP, Xiang HM, *et al*. Preparation, mechanical, and thermal properties of a promising thermal barrier material: Y₄Al₂O₉. *J Adv Ceram* 2015, **4**: 94–102.

[20] Morán-Ruiz A, Vidal K, Larrañaga A, *et al*. Characterization of Ln₄Al₂O₉ (Ln = Y, Sm, Eu, Gd, Tb) rare-earth aluminates as novel high-temperature barrier materials. *Ceram Int* 2018, **44**: 8761–8767.

[21] Lee KN. Environmental barrier coatings for SiC_f/SiC. In *Ceramic Matrix Composites*. Hoboken, NJ, USA: John Wiley & Sons, Inc., 2014: 430–451.

[22] Yamane H, Ogawara K, Omori M, *et al*. Thermal expansion and athermal phase transition of Y₄Al₂O₉ ceramics. *J Am Ceram Soc* 1995, **78**: 1230–1232.

[23] Gervais M, Douy A. Solid phase transformation and metlting of the compounds Ln4Al2O9 (Ln, Gd, Dy, Y). *Mater Sci Eng: B* 1996, **38**: 118–121.

[24] Yamane H, Sakamoto T, Kubota S, *et al*. Preparation and phase transition of Gd₄(Al₁₋ₓGaₓ)₂O₉ solid solutions. *J*

Mater Sci 2001, **36**: 307–311.

[25] Yamane H, Ogawara K, Omori M, *et al*. Phase transition of rare-earth aluminates (RE4Al$_2$O$_9$) and rare-earth gallates (RE$_4$Ga$_2$O$_9$). *J Am Ceram Soc* 1995, **78**: 2385–2390.

[26] Rost CM, Sachet E, Borman T, *et al*. Entropy-stabilized oxides. *Nat Commun* 2015, **6**: 8485.

[27] Chen KP, Pei XT, Tang L, *et al*. A five-component entropy-stabilized fluorite oxide. *J Eur Ceram Soc* 2018, **38**: 4161–4164.

[28] Miracle DB, Senkov ON. A critical review of high entropy alloys and related concepts. *Acta Mater* 2017, **122**: 448–511.

[29] Yan XL, Constantin L, Lu YF, *et al*. (Hf$_{0.2}$Zr$_{0.2}$Ta$_{0.2}$Nb$_{0.2}$Ti$_{0.2}$)C high-entropy ceramics with low thermal conductivity. *J Am Ceram Soc* 2018, **101**: 4486–4491.

[30] Zhao ZF, Xiang HM, Dai FZ, *et al*. (La$_{0.2}$Ce$_{0.2}$Nd$_{0.2}$Sm$_{0.2}$Eu$_{0.2}$)$_2$Zr$_2$O$_7$: A novel high-entropy ceramic with low thermal conductivity and sluggish grain growth rate. *J Mater Sci Technol* 2019, **35**: 2647–2651.

[31] Zhao ZF, Chen H, Xiang HM, *et al*. (Y$_{0.25}$Yb$_{0.25}$Er$_{0.25}$Lu$_{0.25}$)$_2$(Zr$_{0.5}$Hf$_{0.5}$)$_2$O$_7$: A defective fluorite structured high entropy ceramic with low thermal conductivity and close thermal expansion coefficient to Al$_2$O$_3$. *J Mater Sci Technol* 2020, **39**: 167–172.

[32] Zhao ZF, Chen H, Xiang HM, *et al*. (La$_{0.2}$Ce$_{0.2}$Nd$_{0.2}$Sm$_{0.2}$Eu$_{0.2}$)PO$_4$: A high-entropy rare-earth phosphate monazite ceramic with low thermal conductivity and good compatibility with Al$_2$O$_3$. *J Mater Sci Technol* 2019, **35**: 2892–2896.

[33] Chen H, Zhao B, Zhao ZF, *et al*. Achieving strong microwave absorption capability and wide absorption bandwidth through a combination of high entropy rare earth silicide carbides/rare earth oxides. *J Mater Sci Technol* 2020, **47**: 216–222.

[34] Dong Y, Ren K, Lu YH, *et al*. High-entropy environmental barrier coating for the ceramic matrix composites. *J Eur Ceram Soc* 2019, **39**: 2574–2579.

[35] Zhao ZF, Xiang HM, Dai FZ, *et al*. (TiZrHf)P$_2$O$_7$: An equimolar multicomponent or high entropy ceramic with good thermal stability and low thermal conductivity. *J Mater Sci Technol* 2019, **35**: 2227–2231.

[36] Zhao ZF, Chen H, Xiang HM, *et al*. High-entropy (Y$_{0.2}$Nd$_{0.2}$Sm$_{0.2}$Eu$_{0.2}$Er$_{0.2}$)AlO$_3$: A promising thermal/environmental barrier material for oxide/oxide composites. *J Mater Sci Technol* 2020, **47**: 45–51.

[37] Leitner J, Voňka P, Sedmidubský D, *et al*. Application of Neumann–Kopp rule for the estimation of heat capacity of mixed oxides. *Thermochimica Acta* 2010, **497**: 7–13.

[38] Barin II. *Thermochemical Data of Pure Substances*. 3rd edn. Germany: VCH Verlagsgesellschaft mbH, 1995.

[39] Parker WJ, Jenkins RJ, Butler CP, *et al*. Flash method of determining thermal diffusivity, heat capacity, and thermal conductivity. *J Appl Phys* 1961, **32**: 1679–1684.

[40] Zhan X, Li Z, Liu B, *et al*. Theoretical prediction of elastic stiffness and minimum lattice thermal conductivity of Y$_3$Al$_5$O$_{12}$, YAlO$_3$ and Y$_4$Al$_2$O$_9$. *J Am Ceram Soc* 2012, **95**: 1429–1434.

[41] Schneider H, Fischer RX, Schreuer J. Mullite: crystal structure and related properties. *J Am Ceram Soc* 2015, **98**: 2948–2967.

[42] Sun ZQ, Zhou YC, Wang JY, *et al*. Thermal properties and thermal shock resistance of γ-Y$_2$Si$_2$O$_7$. *J Am Ceram Soc* 2008, **91**: 2623–2629.

[43] Sun ZQ, Li MS, Zhou YC. Thermal properties of single-phase Y$_2$SiO$_5$. *J Eur Ceram Soc* 2009, **29**: 551–557.

[44] Lu MH, Xiang HM, Feng ZH, *et al*. Mechanical and thermal properties of Yb$_2$SiO$_5$: A promising material for T/EBCs applications. *J Am Ceram Soc* 2016, **99**: 1404–1411.

[45] Wang SB, Lu YR, Chen YX. Synthesis of single-phase β-Yb$_2$Si$_2$O$_7$ and properties of its sintered bulk. *Int J Appl Ceram Technol* 2015, **12**: 1140–1147.

[46] Slack GA. Nonmetallic crystals with high thermal conductivity. *J Phys Chem Solids* 1973, **34**: 321–335.

[47] Slack GA. The thermal conductivity of nonmetallic crystals. *Phys Rev B Solid State* 1979, **34**: 1–71.

[48] Toberer ES, Zevalkink A, Snyder GJ. Phonon engineering through crystal chemistry. *J Mater Chem* 2011, **21**: 15843–15852.

[49] Chung JD, McGaughey AJH, Kaviany M. Role of phonon dispersion in lattice thermal conductivity modeling. *J Heat Transf* 2004, **126**: 376–380.

[50] Klemens PG. The scattering of low-frequency lattice waves by static imperfections. *Proc Phys Soc A* 1955, **68**: 1113–1128.

[51] Dai FZ, Wen B, Sun YJ, *et al*. Theoretical prediction on thermal and mechanical properties of high entropy (Zr$_{0.2}$Hf$_{0.2}$Ti$_{0.2}$Nb$_{0.2}$Ta$_{0.2}$)C by deep learning potential. *J Mater Sci Technol* 2020, **43**: 168–174.